Virtual materials testing of ASSB cathodes combining AI-based stochastic 3D modeling and numerical simulations

A. Dufter[1*], S. Weber[1], O. Furat[1,2], J. Schubert[3], R. Rekers[3], M. Luczak[4], E. Glatt[4], A. Wiegmann[4], A. Bielefeld[3] and V. Schmidt[1]

[1] *Institute of Stochastics, Ulm University, Helmholtzstraße 18, 89069 Ulm, Germany*
[2] *SDU Applied AI and Data Science Unit, University of Southern Denmark, Campusvej 55, 5230 Odense, Denmark*
[3] *Center for Materials Research (ZfM), Justus Liebig University Giessen, Heinrich-Buff-Ring 16, Giessen 35392, Germany*
[4] *Math2Market GmbH, Richard-Wagner-Straße 1, 67655 Kaiserslautern, Germany*

[*]Corresponding author. *Email address:* anina.dufter@uni-ulm.de (Anina Dufter)

Abstract

The performance of all-solid-state battery (ASSB) cathodes strongly depends on their microstructure. Optimizing the cathode morphology can therefore enhance effective macroscopic properties such as ionic and electronic conductivity. The search for optimized microstructures can be facilitated by virtual materials testing, i.e., by integrating image analysis and stochastic microstructure modeling to generate a wide range of realistic 3D microstructures and evaluate their effective macroscopic properties by means of numerical simulations, thereby reducing the need for extensive physical experiments. This approach allows for the investigation of structure-property relationships through parametric regression models that incorporate relevant geometrical descriptors of 3D microstructures such as volume fractions, mean geodesic tortuosities, specific surface areas, and constrictivities. By linking these geometrical descriptors to effective macroscopic properties, virtual materials testing provides quantitative insight into how microstructure influences material performance. In this paper, this framework is applied to ASSB cathodes. In addition, by systematically varying model parameters, a broad range of 3D microstructures can be generated, which remain close to the original cathode morphology while inducing targeted changes in selected geometrical descriptors. The resulting database enables the calibration of regression models whose predictive performance is assessed by comparing predicted and simulated effective properties such as the ionic and electronic conductivity, thereby quantifying how accurately combinations of geometrical descriptors can explain and predict variations in effective macroscopic properties.

Keywords: Spatial stochastic model, all-solid-state battery, cathode, 3D image data, structure-property-relationship, regression, conductivity, virtual materials testing.

1 Introduction

Lithium-ion batteries are extensively employed due to their high energy density, low mass, and low self-discharge rate, and have increasingly become a key technology in electromobility [1, 2]. Nevertheless, the reliance on flammable liquid electrolytes raises significant safety concerns, while challenges such as dendrite formation, electrolyte leakage, and intrinsic limitations in capacity and energy density remain [3]. All-solid-state batteries (ASSBs), in which liquid electrolytes are replaced by solid-state counterparts, present a promising alternative by offering enhanced safety, superior thermal stability, and extended service life [3–5]. However, challenges such as insufficient ionic conductivity and high interfacial resistance remain to be addressed [6–8].

These limitations are strongly influenced by the microstructure of the battery components, particularly, the microstructure of the electrodes and the interfaces between phases such as the active material and solid electrolyte. In this context, the microstructure of materials, which can be characterized using advanced imaging techniques, plays a crucial role in determining their effective properties and is therefore a key focus of ongoing research [9–12]. For ASSB cathodes this has been extensively studied in [13]. To characterize such microstructures, commonly employed imaging methods include computed electron tomography, computed X-ray tomography—such as nano-CT and micro-CT—and focused ion beam scanning electron microscopy (FIB-SEM) [14–16]. These techniques enable high-resolution two- or three-dimensional reconstructions of the underlying microstructure, allowing the computation of geometrical descriptors of the microstructure such as volume fractions, surface areas, tortuosities, and constrictivities [17].

Since the geometry of the microstructure significantly affects effective macroscopic properties, understanding the relationships between microstructure and macroscopic properties is of considerable interest [18–20]. Optimizing material properties typically requires exploring a vast space of material combinations and microstructures. In the context of ASSB cathodes, relevant properties include ionic and electronic transport, mechanical contact, and interfacial stability [21]. Conducting such investigations purely through experimental testing can be extremely time-consuming and costly. Therefore, virtual ASSB microstructures offer a valuable alternative and play a crucial role in ASSB research [13, 22, 23]. The concept of virtual material testing [24] is built on such virtual microstructures, enabling the systematic analysis of structure-property relationships without the high costs associated with large production volumes and imaging of samples manufactured under varying process conditions [20]. In contrast to a fully experimental approach, only a small number of samples is required. These are used to calibrate a parametric stochastic 3D model based on methods from stochastic geometry [25, 26]. Once calibrated, the model can be regarded as a digital twin and allows for the generation of virtual, but realistic structures that are ideally statistically equivalent to the experimentally measured counterparts [25, 27, 28]. To quantitatively validate the model, geometrical descriptors such as the volume fraction or the specific surface area are computed for the tomographic image data and compared those computed for the model realizations [29, 30].

Using a database of virtual yet physically realistic microstructures, effective macroscopic properties—specifically ionic and electronic conductivity in ASSBs—can be predicted by means of numerical simulations [19, 20]. Such numerical simulations have been employed, for example in [31], where effective electronic and ionic conductivities in lithium-ion batteries were investigated through both numerical and experimental analysis, examining the relationship between porous electrode structure and effective transport properties. Numerical simulations of effective properties form the basis for predictive models that relate geometrical descriptors to macroscopic transport behavior [19, 32, 33]. To this end, regression-based prediction formulas [32, 34, 35] incorporating multiple geometrical descriptors are employed to systematically investigate the influence of microstructure on effective properties. Previous studies have shown that several geometrical descriptors such as volume fraction, tortuosity and constrictivity of the transport phase are well suited for this purpose [18, 19].

Building on this idea and aiming to extend this concept to ASSB microstructures, we apply an approach that combines so-called generative adversarial networks (GANs) [36] with a slightly simplified version of a stochastic geometry model introduced in [37]. This approach overcomes the limitations of GANs—namely their restricted capability for systematic parameter variation due to numerous and often uninterpretable model parameters (i.e., the set of trainable weights)—as well as those of stochastic geometry models, which may struggle to capture highly complex morphologies. This model has been fitted in [37] to three experimentally measured ASSB cathodes composed of identical constituent materials, differing only in the preparation of the solid electrolyte (SE), specifically the milling media used to produce different SE particle systems [38]. These fitted models form the foundation for systematic parameter variation and the generation of a diverse database of virtual 3D realizations. In stochastic models, the volume fraction can often be controlled directly, allowing for the generation of microstructures that exhibit approximately uniformly distributed volume fractions [19, 30]. However, selecting model parameters such that the generated microstructures attain prescribed values of certain geometrical descriptors—particularly those closely related to transport processes, such as geodesic tortuosity and constrictivity—remains challenging. This limitation applies in particular to more complex stochastic 3D models, such as the one employed in the present work. To address this challenge while still ensuring that the resulting scenarios are within the scope of realistic ASSB cathode microstructures, a two-step gradient-based approach is introduced, that, to the best of our knowledge, has not been previously applied in this context. Subsequently, regression-based prediction formulas—which have not been widely investigated for ASSBs—can be explored after computing ionic and electronic conductivities.

These structure-property relationships can provide the foundation for inverse microstructure design, which seeks to determine geometrical descriptors required to achieve targeted effective macroscopic properties, such as high ionic conductivity, sufficient electronic conductivity, and low tortuosity. Rather than predicting transport properties from a given microstructure, the relationship is inverted and formulated as an optimization problem to identify optimal geometrical descriptor ranges and model parameters that yield the desired effective macroscopic properties. Inverse materials design has been applied, for instance, in [39], which introduces a framework for the development of lithium metal battery architectures by combining high-throughput phase-field simulations with machine-learning-based optimization techniques. Through a systematic exploration of electrode and separator design variables, the study identifies the fundamental mechanisms influencing dendrite growth and their impact on overall cell performance. In this context, the present work contributes by establishing robust quantitative structure-property relationships, thereby providing a necessary basis for future inverse microstructure design approaches.

The rest of the paper is structured as follows. First, in Section 2, the materials used in the construction of the three ASSB cathodes are briefly described, along with a description of the stochastic geometry model used in this study. Subsequently, several geometrical descriptors relevant to effective conductivity are discussed, and the regression models used to analyze structure-property relationships are introduced. Additionally, a methodology for generating the large database of virtual ASSB cathodes is presented that combines interpolation and gradient-based

approaches. The results obtained from these methods are presented in Section 3 and discussed in Section 4. Finally, in Section 5, the paper concludes with a summary of the main findings.

2 Materials and methods

To begin with, Section 2.1 provides a brief overview of the investigated cathode materials and the corresponding image data acquisition procedures. Then, in Sections 2.2 and 2.3, we introduce the stochastic 3D model and geometrical descriptors used to characterize microstructures obtained from tomographic imaging. Subsequently, in Sections 2.4, an approach combining parameter interpolation and gradient-based methods is described, which facilitates the generation of a large database of virtual, but realistic ASSB cathode microstructures. Finally, in Sections 2.5 and 2.6, effective macroscopic properties—namely ionic and electronic conductivities—are considered together with regression models that relate geometrical descriptors to effective properties, enabling a quantitative analysis of transport properties.

2.1 Description of material and data acquisition

In this section, we briefly present the ASSB cathode materials used for the acquisition of experimentally measured image data. The ASSB cathodes considered in this paper consist of three phases, namely the solid electrolyte (SE), the active material (AM), and the pore space (P). Specifically, glassy $Li_3PS_4 - 0.5\,LiI$ is used as the SE and $LiNi_{0.83}$, while $Mn_{0.06}Co_{0.11}O_2$ serves as the AM [38]. The three data sets considered in this work were obtained by varying the milling media in a planetary ball mill (Pulverisette 7, Fritsch, Germany) to produce different SE particle systems. The milling media diameters were chosen as 1 mm, 3 mm and 10 mm. The resulting data sets from combining these SE particle systems with the AM are referred to as BM01, BM03 and BM10, respectively.

The microstructure of these three ASSB cathodes have been measured using plasma focused ion beam scanning electron microscopy (PFIB-SEM), which is an advanced imaging and sample preparation technique. PFIB-SEM combines plasma ion beam milling (PFIB), which precisely removes material to expose internal structures, with scanning electron microscopy (SEM) providing high-resolution images of the sample surface. This approach enables precise cross-sectioning and 3D reconstruction of complex materials allowing accurate characterization of microstructural features. The resulting 3D images of the ASSB cathode microstructures have a resolution of 0.1 µm and have been segmented into the three phases, namely the SE and AM as well as the remaining pore space P. For computational purposes, the images are rescaled to a voxel size of 0.2 µm. We refer to [38] for more details regarding material composition and imaging.

Note that during fabrication, ASSB cathode powders are pressed uniaxially into cylindrical half-cells, without binders or conductive additives. As a result, microstructural characteristics may depend on direction, so the cathode cannot be assumed to be isotropic in 3D. For the ASSB cathodes studied, the pressing direction aligns with the z-axis, and inspection of 2D sections shows that the structure differs for differently oriented planes, indicating anisotropy along the z-axis. However, sections parallel to the x-y-plane appear statistically similar under rotation around the z-axis, suggesting cylindrical isotropy to be a reasonable approximation in-plane. See [37] for more details on the investigation of anisotropy with respect to the data sets BM01, BM03 and BM10.

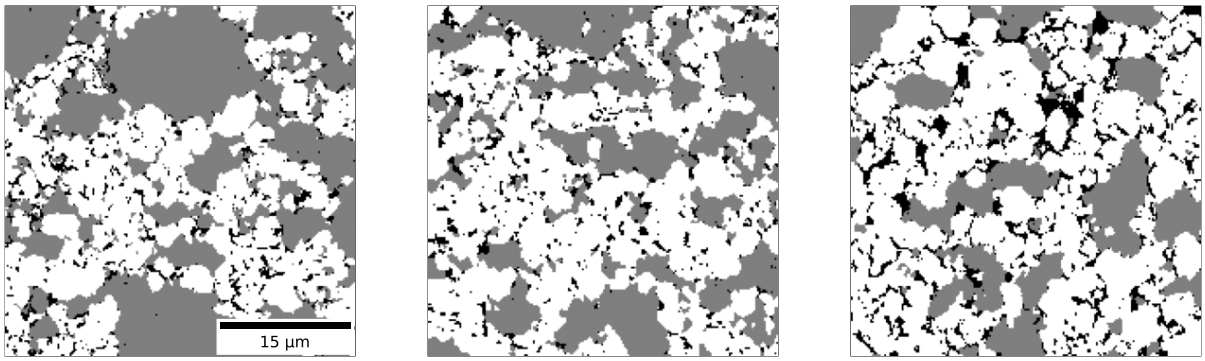

Figure 1: Exemplary chosen 2D sections of the experimentally measured 3D images of BM01 (a), BM03 (b) and BM10 (c). The AM, the SE and the pore space P are represented in white, gray and black, respectively.

2.2 Stochastic 3D model

In this section, the framework for modeling the microstructure of ASSB cathodes is presented, where we employ the parametric stochastic 3D modeling approach introduced in [37], with the simplification that the model parameter γ, controlling the degree of correlation between the underlying random fields, is fixed at 0. This is consistent with the estimated values of γ for the three experimentally acquired image data sets BM01, BM03 and BM10. Thus, the modified model is characterized by a parameter vector $\theta \in \Theta$, where $\Theta = (0,\infty)^5 \times \mathbb{R}^2$ denotes the set of potentially permissible parameter vectors.

Random fields The stochastic 3D model is constructed in two steps. First, two random fields $X = \{X(t)\colon t \in \mathbb{R}^3\}$ and $Y = \{Y(t)\colon t \in \mathbb{R}^3\}$ are considered, given by

$$X = X' + X'' \quad \text{and} \quad Y = Y' + Y'', \tag{1}$$

where X'' and Y'' are Gaussian random fields (GRFs) which are normalized, i.e., $\mathbb{E}X''(t) = \mathbb{E}Y''(t) = 0$ and $\mathrm{VarX''(t)} = \mathrm{VarY''(t)} = 1$ for each $t \in \mathbb{R}^3$, motion invariant (stationary and isotropic) and independent of each other. Furthermore, they are independent of two motion invariant χ^2-fields X' and Y' with n degrees of freedom for some $n \in \mathbb{N} = \{1, 2, \ldots\}$. Thus, the latter two random fields are given by

$$X' = \sum_{j=1}^{n} X_{c,j}^2 \quad \text{and} \quad Y' = \sum_{j=1}^{n} Y_{c,j}^2, \tag{2}$$

where $X_{c,j}, Y_{c,j}, j = 1, \ldots, n$ are independent copies of two normalized independent GRFs $\tilde{X}$ and $\tilde{Y}$, respectively.

Each of the normalized, motion invariant GRFs $\tilde{X}, \tilde{Y}, X''$ and Y'' can be uniquely characterized by its covariance function. In particular, for each of these GRFs we choose the same parametric family of functions to describe their underlying covariance function. Namely, $\rho_\alpha\colon [0,\infty) \to [0,1]$, with

$$\rho_\alpha(h) = \mathrm{e}^{-(\alpha \mathrm{h})^2} \tag{3}$$

for each $h \geq 0$, where $\alpha \in (0,\infty)$ is a model parameter, which we refer to as the covariance parameter. From here on, we denote the covariance parameters of the GRFs $\tilde{X}, \tilde{Y}, X''$, and Y'' by $\alpha_{\tilde{X}}, \alpha_{\tilde{Y}}, \alpha_{X''}$, and $\alpha_{Y''}$, respectively. The relatively simple form of the covariance function given in Eq. (3) is intentionally selected, as it facilitates systematic parameter variation in the parameter study.

Random sets In the second step, by combining the modeling elements introduced above, the stochastic 3D model for the microstructure of ASSB cathodes is given by the mapping $\Xi\colon \mathbb{R}^3 \times \{1,2,3\} \to \{0,1\}$, such that $\{\Xi(t,1), t \in \mathbb{R}^3\}, \{\Xi(t,2), t \in \mathbb{R}^3\}$ and $\{\Xi(t,3), t \in \mathbb{R}^3\}$ represent the solid electrolyte, active material, and pore space, respectively. Formally, it applies

$$\Xi(t,1) = \begin{cases} 1, & \text{if } X(t) \geq \lambda_X, \\ 0, & \text{else,} \end{cases} \tag{4}$$

$$\Xi(t,2) = \begin{cases} 1, & \text{if } \Xi(t,1) = 0 \text{ and } Y(t) \geq \lambda_Y, \\ 0, & \text{else,} \end{cases} \tag{5}$$

$$\Xi(t,3) = 1 - \Xi(t,1) - \Xi(t,2) \tag{6}$$

for each $t \in \mathbb{R}^3$, where $\lambda_X, \lambda_Y \in \mathbb{R}$ are some threshold parameters. Thus, locations $t \in \mathbb{R}^3$ with $\Xi(t,1) = 1$ are associated with the solid electrolyte, those with $\Xi(t,2) = 1$ with the active material, and those with $\Xi(t,3) = 1$ with pore space. In other words, the stationary and isotropic random sets

$$\Xi_{\mathrm{SE}} = \{t \in \mathbb{R}^3\colon \Xi(t,1) = 1\}, \quad \Xi_{\mathrm{AM}} = \{t \in \mathbb{R}^3\colon \Xi(t,2)) = 1\}, \quad \Xi_{\mathrm{P}} = \{t \in \mathbb{R}^3\colon \Xi(t,3) = 1\} \tag{7}$$

represent the three cathode phases SE, AM and P, respectively.

Parameter space In summary, we can state that the stochastic 3D model Ξ described above comprises six model parameters in total: the threshold parameters λ_X and λ_Y, as well as the parameters $\alpha_{\tilde{X}}, \alpha_{\tilde{Y}}, \alpha_{X''}$, and $\alpha_{Y''}$ of the covariance functions of the normalized, motion invariant GRFs $\tilde{X}, \tilde{Y}, X''$ and Y''. However, recall that some small anisotropy effects can be observed in the experimentally measured data sets BM01, BM03, and BM10 with respect to the z-direction, see Section 2.1. To account for this, anisotropy is introduced by scaling the originally isotropic

model Ξ along the z-axis, see [37]. The corresponding scaling parameter is denoted by $a > 0$. Thus, the parameter vector $\theta \in \Theta$ of the (scaled) stochastic 3D model is given by

$$\theta = (\alpha_{\tilde{X}}, \alpha_{\tilde{Y}}, \alpha_{X''}, \alpha_{Y''}, a, \lambda_X, \lambda_Y) \in \Theta = (0, \infty)^5 \times \mathbb{R}^2. \tag{8}$$

To keep the notation simple, for the scaled stochastic 3D model and the corresponding random sets introduced above, we use the same symbols as before, i.e., $\Xi, \Xi_{\mathrm{SE}}, \Xi_{\mathrm{AM}}, \Xi_{\mathrm{P}}$, respectively.

Model calibration In [37], machine learning methods (so-called GANS) have been used to calibrate the stochastic 3D model described above to the three experimentally measured image datasets BM01, BM03, and BM10 presented in Section 2.1, see Table 1. In particular, the calibration approach proposed in [37] is based solely on 2D image data, which is advantageous in situations where only such data is available.

Table 1: Numerical values of the parameter vector $\theta = (\alpha_{\tilde{X}}, \alpha_{\tilde{Y}}, \alpha_{X''}, \alpha_{Y''}, a, \lambda_X, \lambda_Y) \in \Theta$ fitted to the experimentally measured datasets BM01, BM03, and BM10.

Dataset	$\alpha_{\tilde{X}}$	$\alpha_{\tilde{Y}}$	$\alpha_{X''}$	$\alpha_{Y''}$	a	λ_X	λ_Y
BM01	0.07	0.13	0.02	0.65	0.92	1.87	-0.26
BM03	0.03	3.29	0.26	0.19	0.94	1.98	-0.30
BM10	0.02	0.70	0.11	0.20	1	2.45	0.04

2.3 Geometrical descriptors and their estimation

We now state some geometrical descriptors of the stationary random sets $\Xi_{\mathrm{SE}}, \Xi_{\mathrm{AM}}, \Xi_{\mathrm{P}}$ introduced in Section 2.2, and explain how they can be estimated from voxelized image data.

Volume fraction One of the most important geometrical descriptors of a stationary random set is its volume fraction. Specifically, we consider the volume fractions $\varepsilon_{\mathrm{SE}}, \varepsilon_{\mathrm{AM}}, \varepsilon_{\mathrm{P}}$ of $\Xi_{\mathrm{SE}}, \Xi_{\mathrm{AM}}, \Xi_{\mathrm{P}}$, representing the three cathode phases SE, AM and P, which are given by $\varepsilon_p = \mathbb{E}(\nu_3(\Xi_p \cap [0,1]^3))$ for $p \in \{\mathrm{SE}, \mathrm{AM}, \mathrm{P}\}$, where ν_3 denotes the three-dimensional (Lebesgue) volume measure. Note that the volume fractions ε_p for $p \in \{\mathrm{SE}, \mathrm{AM}, \mathrm{P}\}$ can be estimated from voxelized image data using the so-called point-count method [40], where the number of voxels belonging to the phase under consideration is divided by the total number of voxels in the sampling window.

Specific surface area Another relevant geometrical descriptor is the specific surface area S_p for $p \in \{\mathrm{SE}, \mathrm{AM}, \mathrm{P}\}$, which describes the expected surface area of Ξ_p per unit volume and is given by $S_p = \mathbb{E}[\mathcal{H}_2(\partial\Xi_p \cap [0,1]^3)]$, where $\mathcal{H}_2$ denotes the two-dimensional (Hausdorff) surface measure in $\mathbb{R}^3$, and $\partial\Xi_p$ is the boundary of Ξ_p. For voxelized 3D image data, S_p can be estimated using an approach presented in [41], which is based on convolution of the image with a $2 \times 2 \times 2$ mask.

Geodesic tortuosity For a certain direction of transport (e.g. in the z-direction) the geodesic tortuosity τ_p of a given material phase Ξ_p for $p \in \{\mathrm{SE}, \mathrm{AM}, \mathrm{P}\}$ is a measure of shortest path lengths and a crucial structural descriptor regarding virtual materials testing due to its influence on effective macroscopic properties such as diffusivity or permeability [18, 19, 24]. It quantifies the length of pathways restricted to the interior of Ξ_p, connecting a predefined starting plane, which is orthogonal to the direction of transport, to a (parallel) target plane, relative to the distance between the two planes. For a formal definition, we refer to [42], where geodesic tortuosity is considered a random variable τ_p that can be determined from voxelized image data by computing the shortest path lengths (in z-direction) between the starting and corresponding target plane, using the Dijkstra algorithm [43]. These path lengths are normalized by the Euclidean distance between the two planes, which implies $\tau_p \geq 1$. Thus, evaluating all admissible paths that originate from points on the starting plane within the phase of interest $p \in \{\mathrm{SE}, \mathrm{AM}, \mathrm{P}\}$ yields a probability distribution of τ_p, where we put particular emphasis on the mean value $\mu(\tau_p)$ and standard deviation $\sigma(\tau_p)$ of τ_p.

Constrictivity To quantify bottleneck effects, a further geometrical descriptor, the so-called constrictivity of stationary random sets, is considered for each of the three phases $p \in \{\mathrm{SE}, \mathrm{AM}, \mathrm{P}\}$. Its definition is based on two different concepts, namely the simulated mercury intrusion porosimetry (SMIP) and the continuous phase size distribution (CPSD). The latter is a function $\mathrm{CPSD}\colon [0,\infty) \to [0,1]$ characterizing the size of the bulges in the random set Ξ_p. More precisely, for a given radius $r \geq 0$, the value of $\mathrm{CPSD}(r)$ corresponds to the volume fraction of the largest subset of Ξ_p that can be covered by (overlapping) balls of radius r, which do not intersect

the complement $\Xi_p^c = \mathbb{R}^3 \setminus \Xi_p$. Furthermore, $r_{\max}$ denotes the largest radius $r \geq 0$ such that $\mathrm{CPSD}(r) \geq \varepsilon_p/2$. The simulated mercury intrusion porosimetry is a function $\mathrm{SMIP}\colon [0,\infty) \to [0,1]$ such that for a given radius $r \geq 0$, the value of $\mathrm{SMIP}(r)$ corresponds to the volume fraction of the largest subset of Ξ_p which can be covered by a ball of radius r that forms an intrusion in a predefined direction (e.g., in the z-direction, that is, from the bottom of a cubical sampling window). Similarly to the definition of $r_{\max}$ introduced above, $r_{\min}$ denotes the largest radius $r \geq 0$ such that $\mathrm{SMIP}(r) \geq \varepsilon_p/2$. Note that $\mathrm{SMIP}(r) \leq \mathrm{CPSD(r)}$ for all $r \geq 0$. The constrictivity β_p of the stationary random set Ξ_p is then given by $\beta_p = (\frac{r_{\min}}{r_{\max}})^2$, where values close to zero indicate strong bottleneck effects, while values close to one indicate almost no restrictions. For further details, we refer to [42]. The values of both the SMIP and the CPSD functions, and consequently the constrictivity β_p, can be estimated from voxelized image data using the concept of morphological opening and the Euclidean distance transform [44, 45].

2.4 Parameter study

Since, as in many practical scenarios, the acquisition of real microstructure data is often limited in both quantity and variability due to the high costs and time constraints associated with production and imaging of material samples, virtual materials testing offers an efficient alternative. Virtual but realistic microstructures are simulated, and their effective macroscopic properties are evaluated through numerical simulations. An important prerequisite for building an extensive database is the availability of a parametric stochastic model, as introduced in Section 2.2, which enables a systematic variation model parameters to generate microstructures that exhibit new, previously unobserved, effective macroscopic properties.

Based on the three experimentally measured data sets BM01, BM03, and BM10 presented in Section 2.1, the goal is to construct a large database of ASSB cathode microstructures that is as diverse as possible with respect to geometrical descriptors, yet reasonably realistic. To achieve this, we proceed in two steps. First, model parameters associated with the three different data sets are interpolated, enabling the generation of virtual microstructures that represent intermediate states between the experimentally observed microstructures. However, the aim is to explore a wider range of virtual but realistic microstructures. Therefore, in a second step, we consider the gradient of a function that maps a parameter vector to the mean geometrical descriptor computed over five independent model realizations. This gradient indicates how changes in the parameters affect the descriptor, enabling purposeful adjustments to the microstructure. As this gradient cannot be computed analytically, it is approximated using difference quotients. Applying this methodology to all interpolated parameter vectors enables a targeted and systematic exploration of the microstructure space beyond purely interpolated states, thereby substantially enlarging the accessible data space.

Interpolation procdure We begin by introducing the interpolation procedure to generate virtual microstructures. To this end, for two data sets $d_1, d_2 \in \{\mathrm{BM01}, \mathrm{BM03}, \mathrm{BM10}\}$ with $d_1 \neq d_2$, we select parameter vectors located on the connecting line between θ_{d_1} and θ_{d_2}, where $\theta_{d_1}, \theta_{d_2} \in \Theta$ are the parameter vectors of the stochastic 3D model calibrated to d_1 and d_2 with Θ denoting the space of admissible parameter vectors, defined as in Section 2.2. For interpolation between the parameter vectors θ_{d_1} and θ_{d_2}, we consider the mapping $\theta_{d_1,d_2}\colon (0,1) \to \Theta$ given by

$$\theta_{d_1,d_2}(t) = \theta_{d_1} + t(\theta_{d_2} - \theta_{d_1}) \in \Theta, \tag{9}$$

for all $t \in (0,1)$ and $d_1, d_2 \in \{\mathrm{BM01}, \mathrm{BM03}, \mathrm{BM10}\}$ with $d_1 \neq d_2$. A schematic visualization of this interpolation approach is shown in Figure 2. For the parameter study performed in this paper, the interpolation parameter $t \in (0,1)$ is chosen such that five equidistant points are obtained between each pair of parameter vectors θ_{d_1} and θ_{d_2}, i.e., $t \in \{\frac{1}{6}, \frac{2}{6}, \ldots, \frac{5}{6}\}$. For each of these vectors $\theta_{d_1,d_2}(t)$ of interpolated parameters, corresponding model realizations are generated, resulting in 3D microstructures of size $80.2\,\mu\mathrm{m} \times 80.2\,\mu\mathrm{m} \times 80.2\,\mu\mathrm{m}$, corresponding to a $401 \times 401 \times 401$ voxel grid.

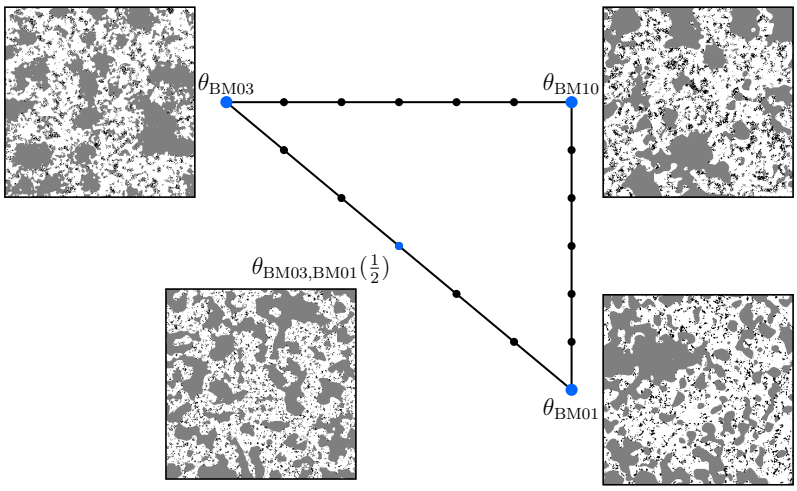

Figure 2: Schematic illustration of the interpolation procedure between the model parameter vectors calibrated to the data sets BM01, BM03 and BM10, where exemplary 2D slices of 3D model realizations are shown for $\theta_{\mathrm{BM01}}, \theta_{\mathrm{BM03}}, \theta_{\mathrm{BM10}}$ and $\theta_{\mathrm{BM03,BM01}}(\frac{1}{2})$.

Gradient-based approach In order to systematically explore further structural scenarios, we consider a gradient-based approach. Although this method can be applied to various geometrical descriptors, for simplicity, the concept is only introduced for the specific surface area of AM. More precisely, a function denoted by $f_{S_{\mathrm{AM}}} \colon \Theta \to [0,\infty)$ is considered, which maps the parameter vector of the stochastic 3D model to the specific surface area of AM. However, the same procedure applies analogously for $S_{\mathrm{SE}}, \varepsilon_p, \mu(\tau_p), \beta_p$ and the corresponding functions $f_{S_{\mathrm{SE}}} \colon \Theta \to [0,\infty)$ as well as $f_{\varepsilon_p} \colon \Theta \to [0,1]$, $f_{\mu(\tau_p)} \colon \Theta \to [1,\infty)$, and $f_{\beta_p} \colon \Theta \to [0,1]$ for $p \in \{\mathrm{AM}, \mathrm{SE}\}$ that map the parameter vector of the stochastic 3D model on the corresponding geometrical descriptors. Note that geometrical descriptors of the pore space are not considered, as the pores exhibit low volume fractions and lack connectivity. Consequently, in this phase, there are no suitable transport pathways available.

Due to variations between model realizations for a given parameter vector $\theta \in \Theta$, the function $f_{S_{\mathrm{AM}}} \colon \Theta \to [0,\infty)$ maps the parameter vector to the mean specific surface area of the AM evaluated over five realizations of the model corresponding to θ, thus reducing the influence of statistical fluctuations and potential outliers. For simplicity, the methodology is illustrated for the connecting line between θ_{d_1} and θ_{d_2}. The same applies analogously to all other connecting lines. To keep the notation simple, in the following we will write $\theta_1, \theta_2, \dots \theta_5$ instead of $\theta_{d_1,d_2}(\frac{1}{6}), \theta_{d_1,d_2}(\frac{2}{6}), \dots, \theta_{d_1,d_2}(\frac{5}{6})$, respectively.

To generate model realizations that exhibit significant variations in the specific surface area of AM, we use a method based on gradient-descent, where, to approximate the gradient, we approximate the directional derivatives of $f_{S_{\mathrm{AM}}}$ at θ_k using a difference quotient. In particular, for each $q \in \{1, \dots, 7\}$, we use a small perturbation $\delta > 0$ in the direction of the standard basis vector $e_q = (0, \dots, 0, 1, 0, \dots, 0) \in \mathbb{R}^7$ to estimate the gradient $(\nabla f_{S_{\mathrm{AM}}})(\theta_k)$ for each $k \in \{1, \dots, 5\}$ by

$$(\nabla f_{S_{\mathrm{AM}}})(\theta_k) \approx \left(\frac{f_{S_{\mathrm{AM}}}(\theta_k + \delta \cdot e_q) - f_{S_{\mathrm{AM}}}(\theta_k)}{\delta} \right)_{q=1}^{7}, \tag{10}$$

where all components of $e_q = (0, \dots, 0, 1, 0, \dots, 0)$ are equal to 0, except the q-th component which is equal to 1. The (approximation of the) gradient given in Eq. (10) provides the direction of the steepest change in $f_{S_{\mathrm{AM}}}$ at θ_k [46] and allows for a systematic generation of virtual microstructures in a neighborhood of θ_k. In particular, in addition to microstructures generated under the parameter vector θ_k, we consider parameter vectors of the form

$$\tilde{\theta}_k(h) = \theta_k + h \cdot (\nabla f_{S_{\mathrm{AM}}})(\theta_k) \tag{11}$$

to generate further virtual microstructures, where the scalar $h \in \mathbb{R}$ controls the step size along the gradient direction. Consequently, the scalar h predominantly allows us to control the descriptor $f_{S_{\mathrm{AM}}}$ of simulated microstructures. Note that, since the anisotropy scaling factor a is very similar for the three experimentally measured datasets, namely $a = 0.92$, $a = 0.94$, and $a = 1$ for BM01, BM03, and BM10, respectively, the component $(\nabla f_{S_{\mathrm{AM}}}(\theta_k))_5$ of the gradient $(\nabla f_{S_{\mathrm{AM}}})(\theta_k)$ corresponding to the anisotropy scaling parameter a is set to zero, i.e., $(\nabla f_{S_{\mathrm{AM}}}(\theta_k))_5 = 0$ for each $k \in \{1, \dots, 5\}$.

The gradient-based methodology stated above can be similarly extended to the specific surface area of the SE, as well as to additional geometrical descriptors, including volume fraction, mean geodesic tortuosity, and constrictivity.

Thus, it provides a framework for systematically generating microstructural variations around a given parameter vector θ_k, allowing for a broader but well-controlled exploration of the parameter space, see Figure 3.

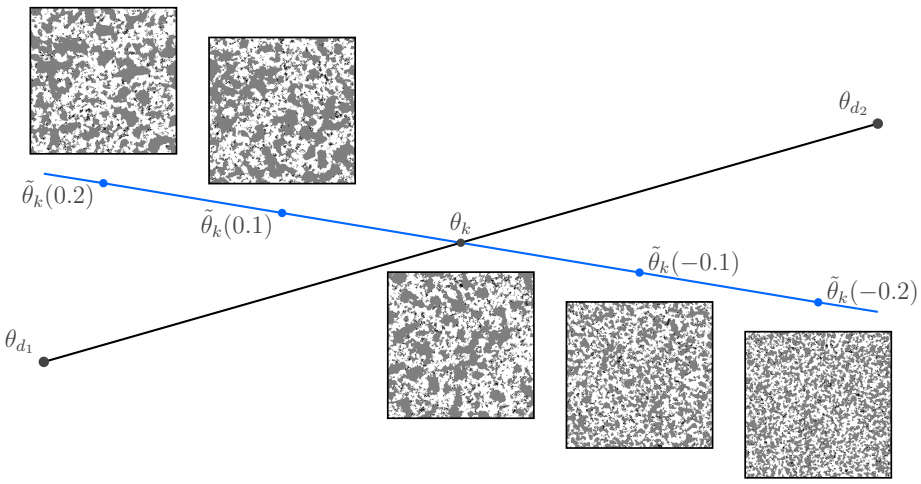

Figure 3: Schematic illustration of the gradient-based approach. The black line corresponds to the interpolation procedure considerd in Eq. (9), and the blue line corresponds to the gradient-based methodology given in Eq. (11).

The incremental parameter shift δ considered in Eq. (10) is set to 0.05. When computing the gradient with respect to the volume fraction, the specific surface area, and the mean geodesic tortuosity, the step size h in Eq. (11) is successively chosen from the set $\{-0.2, -0.1, 0.1, 0.2\}$. For constrictivity, smaller values of h from the set $\{-0.05, -0.025, 0.025, 0.05\}$ are used, as larger step sizes lead to unrealistic cathode microstructures. To further ensure physical plausibility, the admissible range of the covariance parameter α considered in Eq. (3) is restricted to the interval $[0.05, \infty)$ for all GRFs $\tilde{X}, \tilde{Y}, X'', Y''$ introduced in Section 2.2. Similarly to θ_k, for each parameter vector $\tilde{\theta}_k(h)$, 3D microstructures are generated of size $80.2\,\mu\text{m} \times 80.2\,\mu\text{m} \times 80.2\,\mu\text{m}$, corresponding to a $401 \times 401 \times 401$ voxel grid. In total a database comprising 495 virtual 3D microstructures is obtained.

2.5 Effective macroscopic properties and their simulation

Note that, similarly to Section 2.3, effective macroscopic properties of (virtual) ASSB cathode microstructures are defined and computed from 3D image data. In particular, note that the governing equations used to define effective macroscopic properties are given on continuous domains, which we denote by $\Omega \subset \mathbb{R}^3$. To numerically compute solutions of the governing equations, the domain Ω is discretized, where the correspondingly discretized transport phases in realizations of the stochastic 3D model Ξ can be considered to be the discretized versions of the domain Ω.

Conductivity Two key effective properties of ASSB cathodes are the ionic and electronic conductivity, describing the ion and electron transport through the composite microstructure. Due to the negligible ionic conductivity of the AM and the negligible electronic conductivity of the SE, transport is modeled by considering only one conducting phase at a time [47]. Under steady-state conditions and assuming electroneutrality as well as the absence of charge accumulation, both electronic and ionic transport can be described within the same mathematical framework. Although electronic conduction is inherently Ohmic and ionic transport originates from Fick's Law [48], the computation of effective ionic and electronic conductivities in microstructure-resolved simulations reduces to solving a steady-state conduction problem in the respective conducting phase. Therefore, the concept is only introduced for the electronic conductivity. Let $\Omega \subset \mathbb{R}^3$ be the continuous domain representing the material phase, where transport occurs. Charge transport is described by Ohm's Law

$$J = -\sigma_0 \nabla U \quad \text{in } \mathring{\Omega}, \tag{12}$$

where $J \colon \Omega \to \mathbb{R}^3$ denotes the current density, $\sigma_0 > 0$ the phase-specific intrinsic conductivity, and $U \colon \Omega \to \mathbb{R}$ the electric potential. Here, $\mathring{\Omega}$ denotes the interior of Ω. Conservation of charge requires

$$\nabla \cdot J = 0 \quad \text{in } \mathring{\Omega}, \tag{13}$$

which yields that

$$\nabla \cdot (\sigma_0 \nabla U) = 0 \quad \text{in } \mathring{\Omega}. \tag{14}$$

Since σ_0 is constant, Eq. (14) reduces to the Laplace equation

$$\nabla^2 U = 0 \quad \text{in } \mathring{\Omega}. \tag{15}$$

Note that Dirichlet boundary conditions are specified on two opposite external surfaces of Ω, assigning U with the value 0 on one surface and 1 on the opposite surface. Zero-flux boundary conditions for U are applied to all remaining surfaces, including both the other external faces as well as the internal interfaces between the conducting phase and its complement. The effective electronic conductivity σ_{eff} is then determined by solving this boundary value problem on the microstructure and relating the respective flux to that of the homogenized problem [28]. As mentioned above, the same mathematical framework applies for the determination of ionic conductivity.

M-factor The M-factor, defined as

$$M = \frac{\sigma_{\text{eff}}}{\sigma_0}, \tag{16}$$

is a useful measure to quantify the influence of microstructure on transport processes. Here, σ_0 is the intrinsic transport coefficient, representing the ideal transport properties of a uniform bulk material. In contrast, the effective transport coefficient σ_{eff} accounts for the actual microstructure geometry and incorporates the impact of obstacles, constrictions, and phase connectivity, effectively scaling σ_0 to reflect real transport conditions. The M-factor can be applied to both ionic and electronic conductivity, making it a versatile tool for characterizing transport in complex cathode microstructures. For a phase with volume fraction ε in which transport occurs, the M-factor satisfies $M \in [0, \varepsilon]$ according to Eq. 21.14 in [49]. Note that in the literature often a similar measure, the so-called τ-factor or effective tortuosity τ_{eff}, is used [50, 51], which is closely related to the M-factor and given by

$$\tau_{\text{eff}} = \varepsilon \frac{\sigma_0}{\sigma_{\text{eff}}} = \frac{\varepsilon}{M} \in [1, \infty). \tag{17}$$

The M-factors for ionic and electronic conductivity, respectively, are computed by numerical homogenization of the voxelized microstructure using GeoDict [52]. In GeoDict, the Laplace equation is solved on a Cartesian grid, and the macroscopic conductivity tensor is obtained from the volume-averaged superficial current density under imposed electrical potential gradients [53].

2.6 Regression models for structure-property relationships

Pairing geometrical descriptor values computed from a set of 3D images with their corresponding M-factors yields a dataset for regression models, enabling the relation of geometrical descriptors to effective macroscopic properties. More precisely, for each phase $p \in \{\text{AM}, \text{SE}\}$ and for each of the 495 microstructures generated in the parameter study as stated in Section 2.4, we consider the pair consisting of the vector $(\varepsilon_{j,p}, S_{j,p}, \mu(\tau_{j,p}), \sigma(\tau_{j,p}), \beta_{j,p}))$ and $m_{j,p}$, where $\varepsilon_{j,p}, S_{j,p}, \mu(\tau_{j,p}), \sigma(\tau_{j,p}), \beta_{j,p}$ denote the volume fraction, the specific surface area, the mean and standard deviation of the geodesic tortuosity and the constrictivity of phase $p \in \{\text{AM}, \text{SE}\}$ for the j-th microstructure with $j \in \{1, \ldots, 495\}$, while $m_{j,p}$ is the M-factor of phase p and the j-th microstructure. For each phase $p \in \{\text{AM}, \text{SE}\}$, this database is then divided into a set of training data containing 331 pairs and a set of test data containing 164 pairs.

Analytical regression formulas Regression models in the form of analytical formulas are considered that will be used to establish microstructure-property relationships, i.e., formulas that enable us to compute various predictors, in the following denoted by $\widehat{M}_1, \ldots, \widehat{M}_4$, of the M-factor from the geometrical descriptors for AM and SE introduced in Section 2.3, where the phase under consideration will be omitted in the notation to keep it possibly simple. Note that several regression models of this type have been proposed in the literature to characterize transport-related structure-property relationships. The simplest approach uses only the volume fraction ε to predict the M-factor. This leads to the predictor $\widehat{M}_1$ of M given by

$$\widehat{M}_{1,C_1}(V_1) = \varepsilon^{c_1}, \tag{18}$$

where $C_1 = c_1 > 0$ and $V_1 = \varepsilon$, see also [54, 55] for some variations of this regression formula. A slightly modified version of a more advanced model, introduced in [35], additionally incorporates further geometrical descriptors, namely the constrictivity β and mean geodesic tortuosity $\mu(\tau)$, which provides the predictor $\widehat{M}_2$ of M given by

$$\widehat{M}_{2,C_2}(V_2) = c_1 \varepsilon^{c_2} \beta^{c_3} \mu(\tau)^{c_4}, \tag{19}$$

with $C_2 = (c_1, c_2, c_3, c_4) \in \mathbb{R}^4$ and $V_2 = (\varepsilon, \beta, \mu(\tau))$. Another model, considered in [19], uses both the mean value $\mu(\tau)$ and the standard deviation $\sigma(\tau)$ of the geodesic tortuosity τ as well as the volume fraction ε, which leads to the predictor $\widehat{M}_3$, where

$$\widehat{M}_{3,C_3}(V_3) = c_1 \mu(\tau)^{c_2} \sigma(\tau)^{c_3} \varepsilon^{c_4}, \tag{20}$$

with $C_3 = (c_1, c_2, c_3, c_4) \in \mathbb{R}^4$ and $V_3 = (\varepsilon, \mu(\tau), \sigma(\tau))$. Furthermore, extending $\widehat{M}_3$ by additionally including the constrictivity β yields

$$\widehat{M}_{4,C_4}(V_4) = c_1 \mu(\tau)^{c_2} \sigma(\tau)^{c_3} \varepsilon^{c_4} \beta^{c_5}, \tag{21}$$

where $C_4 = (c_1, c_2, c_3, c_4, c_5) \in \mathbb{R}^5$ and $V_4 = (\varepsilon, \mu(\tau), \sigma(\tau))$.

Fitting of model parameters The parameters $c_1, \ldots, c_5$ of the regression models stated above are estimated by least squares optimization using Scipy's `minimize` function with the L-BFGS-B algorithm [56]. Specifically, the objective function to be minimized is given by

$$g(C_i) = \sum_{j=1}^{n_{\text{train}}} \left(m_j - \widehat{M}_{i,C_i}(V_{i,j}) \right)^2, \tag{22}$$

where $m_1, \ldots, m_{n_{\text{train}}}$ denotes the sample of numerically computed M-factors, $\widehat{M}_{i,C_i}(V_{i,1}), \ldots, \widehat{M}_{i,C_i}(V_{i,n_{\text{train}}})$ the corresponding predictions of model $\widehat{M}_i$ for $i \in \{1, \ldots, 4\}$, and $n_{\text{train}} \in \mathbb{N}$ the number of data points considered (here, $n_{\text{train}} = 331$).

Error measures for model validation In order to evaluate the predictive capabilities of the regression models $\widehat{M}_1, \ldots, \widehat{M}_4$, the mean absolute percentage error (MAPE) between the predicted and numerically computed M-factors and the coefficient of determination R^2 are considered, as they quantify complementary aspects of model quality, namely the average percentage error between predicted and simulated values as well as the explained variance. For simplicity, the abbreviating notation $\widehat{m}_{i,j} = \widehat{M}_{i,C_i}(V_{i,j})$ for $i \in \{1, \ldots 4\}$ and $j \in \{1, \ldots, n_{\text{test}}\}$ is used in the following, where $n_{\text{test}} \in \mathbb{N}$ (here, $n_{\text{test}} = 164$) denotes the number of data points considered. Then, for each $i \in \{1, \ldots, 4\}$, the MAPE_i of the i-th regression model $\widehat{M}_i$ is defined as

$$\text{MAPE}_i = \frac{100}{n_{\text{test}}} \sum_{j=1}^{n_{\text{test}}} \left| \frac{\widehat{m}_{i,j} - m_j}{m_j} \right|. \tag{23}$$

Smaller MAPE values indicate a higher predictive accuracy, with a value of zero corresponding to perfect agreement. Additionally, the coefficient of determination $R^2 \in [0, 1]$ is evaluated according to

$$R_i^2 = 1 - \frac{\sum_{j=1}^{n_{\text{test}}} (m_j - \widehat{m}_{i,j})^2}{\sum_{j=1}^{n_{\text{test}}} (m_j - \bar{m})^2} \tag{24}$$

for each $i \in \{1, \ldots 4\}$, where $\bar{m}$ denotes the arithmetic mean of the numerically determined sample $m_1, \ldots, m_{n_{\text{test}}}$ of M-factors. Values of R^2 close to one indicate a strong explanatory power of the model, whereas values close to zero reflect limited predictive capability.

3 Results

This section presents results of the parameter study introduced in Section 2.4, as well as structure-property relationships obtained for the regression models $\widehat{M}_1, \ldots, \widehat{M}_4$ stated in Section 2.6, using measured and simulated 3D microstructures of ASSB cathodes. Recall that the stochastic 3D model stated in Section 2.2 forms the basis of the parameter study, where the parameter vector $\theta = (\alpha_{\tilde{X}}, \alpha_{\tilde{Y}}, \alpha_{X''}, \alpha_{Y''}, a, \lambda_X, \lambda_Y) \in \Theta$ of this model has been fitted to the three experimentally measured image datasets BM01, BM03, and BM10 presented in Section 2.1, using machine learning methods (so-called GANs) proposed in [37], see Table 1.

The corresponding values of geometrical descriptors and the M-factor are shown in Table 2. Although volume fractions and mean geodesic tortuosities of BM01 and BM03 vary only slightly for AM and SE, more pronounced differences are observed for the constrictivity β_{SE} and the specific surface area S_{SE}. These discrepancies can be

attributed to the different milling media used during the production of the SE particle systems of BM01 and BM03, see Section 2.1. For the same reason, only minor variations are observed for most of the geometrical descriptors of the AM of BM01 and BM03. However, most of the geometrical descriptors of BM10 differ significantly from those of BM01 and BM03. Furthermore, the highest M-factor is obtained for the AM in BM10, while for the SE it is achieved in BM03.

Table 2: Geometrical descriptors and M-factors computed for the experimentally measured datasets BM01, BM03, and BM10.

Dataset	$\varepsilon_{\mathrm{AM}}$	$\varepsilon_{\mathrm{SE}}$	$\mu(\tau_{\mathrm{AM}})$	$\mu(\tau_{\mathrm{SE}})$	β_{AM}	β_{SE}	$S_{\mathrm{AM}}\,[\mu\mathrm{m}^{-1}]$	$S_{\mathrm{SE}}\,[\mu\mathrm{m}^{-1}]$	M_{AM}	M_{SE}
BM01	0.52	0.41	1.07	1.12	0.72	0.38	1.00	0.80	0.32	0.13
BM03	0.51	0.42	1.07	1.13	0.75	0.51	0.85	0.65	0.35	0.21
BM10	0.56	0.34	1.06	1.20	0.91	0.13	0.85	0.35	0.41	0.08

3.1 Examples of virtual microstructures of ASSB cathodes

We first present eight examples of the 495 ASSB cathode microstructures, which have been generated using the interpolation procedure together with the gradient-based approach introduced in Section 2.4. The parameter vectors $\theta = (\alpha_{\tilde{X}}, \alpha_{\tilde{Y}}, \alpha_{X''}, \alpha_{Y''}, a, \lambda_X, \lambda_Y) \in \Theta$ considered for these examples are listed in Table 3. Note that for some components of θ, the values given in Table 3 are close to those given in Table 1 for the experimentally measured image datasets BM01, BM03, and BM10, whereas these values are rather different for other components of θ. Planar cross-sections of the eight examples of simulated 3D microstructures are shown in Figure 4.

Table 3: Values of the components of the parameter vector $\theta = (\alpha_{\tilde{X}}, \alpha_{\tilde{Y}}, \alpha_{X''}, \alpha_{Y''}, a, \lambda_X, \lambda_Y) \in \Theta$ that have been used to generate eight examples of the 495 (virtual) 3D microstructures of ASSB cathodes.

Subfigure	$\alpha_{\tilde{X}}$	$\alpha_{\tilde{Y}}$	$\alpha_{X''}$	$\alpha_{Y''}$	a	λ_X	λ_Y
a	0.05	0.41	0.07	0.43	0.96	2.16	-0.11
b	0.15	0.32	0.07	0.50	0.95	2.06	-0.16
c	0.05	0.32	0.05	0.50	0.95	2.06	-0.16
d	0.15	1.18	0.13	0.50	0.93	1.90	-0.27
e	0.05	1.17	0.08	0.48	0.93	1.82	-0.26
f	0.33	0.47	0.05	0.39	0.92	1.70	-0.45
g	0.05	1.11	0.23	0.21	0.99	2.38	-0.04
h	0.10	1.56	4.86	0.18	0.98	2.29	-0.07

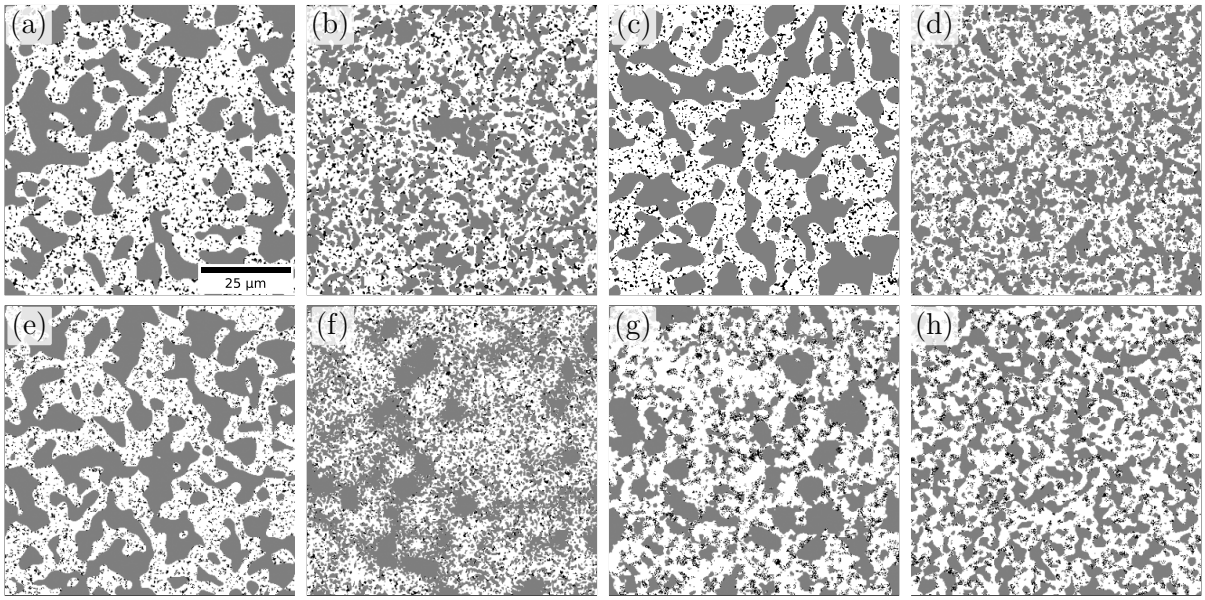

Figure 4: Planar cross-sections of simulated 3D microstructures of ASSB cathodes, where the AM, the SE and the pore space P are represented in white, gray and black, respectively.

Furthermore, the corresponding geometrical descriptors and M-factors computed for the AM and SE of the eight examples of simulated 3D microstructures are displayed in Table 4. The finer structure of the SE, visible in Figures 4b, 4d, 4f and 4h is reflected in the specific surface area S_{SE} with values larger than 0.6 as well as increased constrictivity β_{SE}. In contrast, Figures 4a and 4c show a coarser SE structure, which corresponds to lower values of S_{SE} (≤ 0.3) and reduced β_{SE}. Furthermore, higher values of λ_X shown in Table 3, such as for the examples shown in Figures 4a, 4g, and 4h, correspond to lower values of the volume fraction $\varepsilon_{\mathrm{SE}}$, and vise versa. Small values of M_{SE}, as for the examples shown in Figures 4g and 4h, correspond to small values of β_{SE} and high values of $\mu(\tau_{\mathrm{SE}})$.

Table 4: Geometrical descriptors and M-factors computed for the eight examples of the 495 (virtual) 3D microstructures of ASSB cathodes.

Subfigure	$\varepsilon_{\mathrm{AM}}$	$\varepsilon_{\mathrm{SE}}$	$\mu(\tau_{\mathrm{AM}})$	$\mu(\tau_{\mathrm{SE}})$	$\sigma(\tau_{\mathrm{AM}})$	$\sigma(\tau_{\mathrm{SE}})$	β_{AM}	β_{SE}	$S_{\mathrm{AM}}\,[\mu\mathrm{m}^{-1}]$	$S_{\mathrm{SE}}\,[\mu\mathrm{m}^{-1}]$	M_{AM}	M_{SE}
a	0.54	0.38	1.05	1.14	0.01	0.04	1.00	0.49	0.92	0.25	0.32	0.12
b	0.53	0.40	1.06	1.12	0.01	0.02	1.00	0.86	1.27	0.81	0.28	0.11
c	0.53	0.40	1.05	1.13	0.01	0.03	0.46	0.54	0.86	0.30	0.31	0.13
d	0.51	0.43	1.06	1.10	0.01	0.01	1.00	0.70	1.34	0.84	0.26	0.15
e	0.49	0.45	1.06	1.10	0.01	0.03	0.51	0.47	0.91	0.33	0.27	0.19
f	0.48	0.47	1.07	1.09	0.01	0.01	1.00	0.98	1.80	1.61	0.22	0.14
g	0.57	0.34	1.05	1.16	0.01	0.03	0.96	0.40	1.24	0.49	0.30	0.06
h	0.55	0.36	1.05	1.14	0.01	0.02	0.99	0.53	1.30	0.62	0.29	0.09

3.2 Empirical distributions of geometrical descriptors

For the set of all 495 virtual 3D ASSB cathode microstructures, generated in the parameter study of Section 2.4, empirical probability distributions of several geometrical descriptors and the M-factor are computed. In particular, the database of virtual 3D microstructures is designed to cover a wide range of geometrical descriptor values and M-factor values, which fluctuate around the values shown in Table 2 that were determined for the respective characteristics of the experimentally measured image data. Figure 5 presents so-called violin plots of volume fraction, mean geodesic tortuosity, constrictivity, and specific surface area, as well as the M-factor, each computed for AM and SE of the 495 virtual 3D ASSB cathode microstructures.

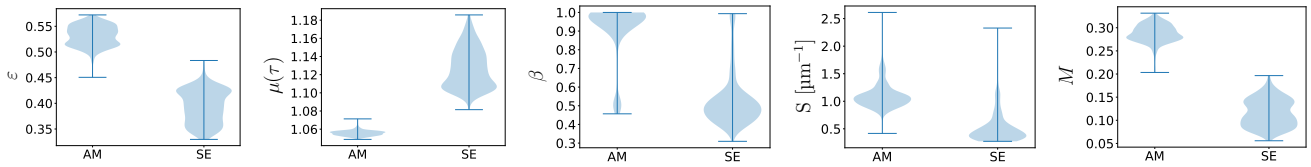

Figure 5: Empirical distributions of (a) volume fraction, (b) mean geodesic tortuosity, (c) constrictivity, (d) specific surface area and (e) M-factor associated with AM and SE for all virtual 3D ASSB cathode microstructures generated in the parameter study.

In particular, the plots presented in Figure 5 show that the volume fraction $\varepsilon_{\mathrm{AM}}$ of AM spans 0.45 to 0.57, while that of SE ranges from 0.33 to 0.48. With respect to the mean geodesic tortuosity, which quantifies the lengths of the shortest transportation paths, only minor variations of approximatively 0.03 are observed for the AM, while $\mu(\tau_{\mathrm{SE}})$ exhibits a wider range from 1.081 to 1.186. The constrictivities β_{AM} and β_{SE} show greater variability for both phases, with most values for AM belonging to the interval $[0.85, 1]$, while those for SE range from 0.31 to 0.99. A similar trend can be seen in the specific surface area, where S_{AM} ranges from $0.42\,\mu\mathrm{m}^{-1}$ to $2.61\,\mu\mathrm{m}^{-1}$ and is predominantly clustered in the range $[0.7\,\mu\mathrm{m}^{-1}, 1.7\,\mu\mathrm{m}^{-1}]$. However, S_{SE} ranges from $0.27\,\mu\mathrm{m}^{-1}$ to $2.33\,\mu\mathrm{m}^{-1}$, with the majority of values belonging to the interval $[0.27\,\mu\mathrm{m}^{-1}, 1.35\,\mu\mathrm{m}^{-1}]$. Finally, the M-factor for AM spans from 0.20 to 0.33 and that for SE from 0.06 to 0.20, indicating that the differences observed in the geometrical descriptors significantly influence the M-factor. For further details, see Section 4.

3.3 Structure-property relationships

The 495 virtual 3D microstructures generated in the parameter study of Section 2.4 are divided into a training dataset comprising 331 microstructures and a test dataset of 164 microstructures. The training dataset is used to calibrate the regression models introduced in Section 2.6. The resulting coefficients $c_1, \ldots, c_5$ of these models are

presented in Table 5 for both AM and SE. In addition, the corresponding MAPE and R^2 values, evaluated on the test dataset, are provided.

Table 5: Coefficients $c_1, \ldots, c_5$ of the regression models $\widehat{M}_1$, $\widehat{M}_2$, $\widehat{M}_3$ and $\widehat{M}_4$ for AM and SE, obtained by least-squares optimization using the training dataset of 331 microstructures. In addition, the corresponding MAPE and R^2 values computed for the test dataset of 164 microstructures are presented.

	AM							SE						
	c_1	c_2	c_3	c_4	c_5	MAPE	R^2	c_1	c_2	c_3	c_4	c_5	MAPE	R^2
$\widehat{M}_1$	1.98					5.13%	0.300	2.32					8.51%	0.843
$\widehat{M}_2$	0.99	0.11	−0.002	−21.52		1.70%	0.897	2.74	3.88	−0.09	3.09		6.08%	0.882
$\widehat{M}_3$	1.10	−19.60	0.03	0.24		1.68%	0.906	3.99	−0.54	0.13	3.26		5.47%	0.912
$\widehat{M}_4$	1.10	−19.60	0.03	0.24	−0.002	1.68%	0.906	4.36	−1.42	0.16	3.08	0.06	5.43%	0.911

The results of all four regression models $\widehat{M}_1$, $\widehat{M}_2$, $\widehat{M}_3$ and $\widehat{M}_4$, computed for AM, are visualized in Figure 6, where the predicted M-factors are plotted against those obtained from numerical simulations, along with the corresponding mean absolute percentage error MAPE and the coefficient of determination R^2.

The regression model $\widehat{M}_1$, given in Eq. (18), which only considers the volume fraction, yields a comparatively low R^2 of 0.300 and a MAPE of approximately 5%, as shown in Figure 6a. Substantial improvement of both error measures is observed for $\widehat{M}_2$, given in Eq. (19), see Figure 6b. In particular, for $\widehat{M}_2$, a value of $R^2 = 0.897$ is achieved for the coefficient of determination, where MAPE = 1.70%. Similar results are obtained for the regression model $\widehat{M}_3$, given in Eq. (20), where additionally to the volume fraction, the mean and standard deviation of the geodesic tortuosity are included, yielding $R^2 = 0.906$ and MAPE = 1.68%, see Figure 6c. Figure 6d shows that with respect to AM the same values are achieved for model $\widehat{M}_4$, stated in Eq. (21), that combines all geometrical descriptors used for $\widehat{M}_2$ and $\widehat{M}_3$.

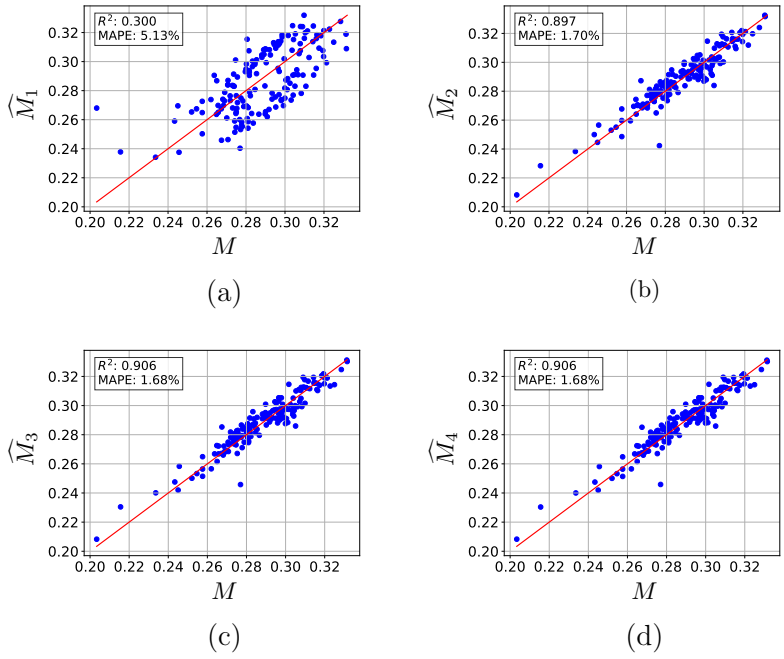

Figure 6: Predicted M-factors over numerically simulated M-factors with respect to AM, for all 164 virtual ASSB cathode microstructures of the test dataset. The red line ($\widehat{M} = M$) serves as reference.

The results of the regression models $\widehat{M}_1$, $\widehat{M}_2$, $\widehat{M}_3$ and $\widehat{M}_4$ fitted to SE are shown in Figure 7. The model $\widehat{M}_1$, given in Eq. (18), which attempts to find a direct connection between the volume fraction $\varepsilon_{\mathrm{SE}}$ and the M-factor, achieves $R^2 = 0.843$ and a MAPE of 8.51%, see Figure 7a, which is significantly better than the corresponding results for AM. The model $\widehat{M}_2$, which additionally incorporates constrictivity and mean geodesic tortuosity, yields $R^2 = 0.882$ and a MAPE of 6.08%, as can be seen in Figure 7b. The models $\widehat{M}_3$ and $\widehat{M}_4$ further increase the coefficient of determination to $R^2 = 0.912$ and 0.911, respectively, while the MAPE decreases to 5.47% and 5.43%, see Figures 7c and 7d.

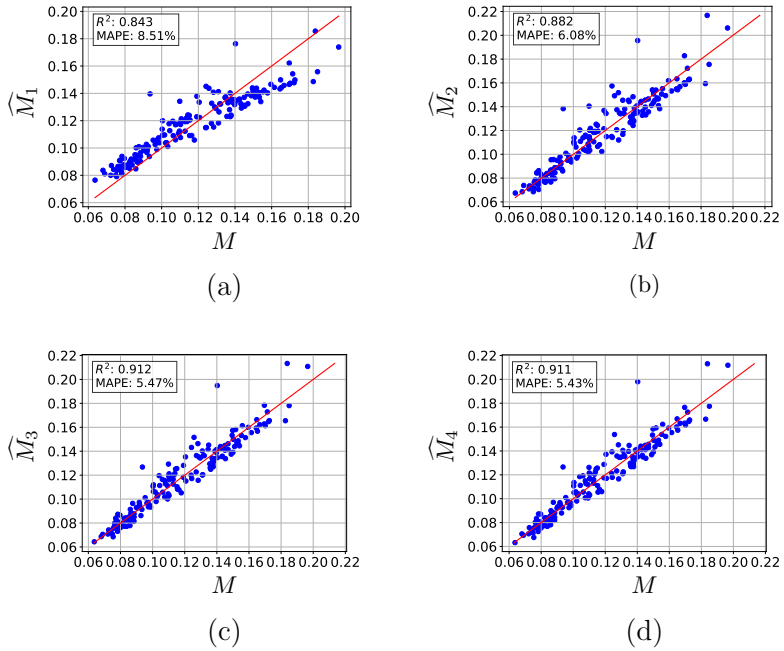

Figure 7: Predicted M-factors over numerically simulated M-factors with respect to SE, for all 164 virtual ASSB cathode microstructures of the test dataset.

4 Discussion

In this section, the methods and results presented in this paper are discussed. Specifically, the methods used to generate a large database of virtual yet realistic ASSB cathode microstructures are evaluated, followed by a discussion of the analysis of the generated image data with respect to several geometrical descriptors. Finally, the results of the fitted regression models are examined in order to quantify and interpret the underlying structure-property relationships.

Database of virtual image data Typically, when aiming to generate a large database of virtual image data based on a parametric stochastic geometry model—particularly for investigating structure-property relationships—the input parameters are systematically varied to cover a broad spectrum of differently structured microstructures. In many cases, the volume fraction of each material phase is directly controlled by a model parameter and therefore can be deliberately adjusted [19]. However, other descriptors—especially those closely related to transport properties, such as geodesic tortuosity and constrictivity—often cannot be controlled explicitly, a limitation that becomes more pronounced for complex stochastic geometry models such as the one employed in the present paper. Consequently, it can be difficult to generate microstructures that both remain close to experimentally measured ones and allow for a controlled variation of specific geometrical descriptors. Therefore, the gradient-based approach proposed in this paper offers a new perspective on systematic parameter variation and generation of large databases of virtual 3D microstructures.

Structural analysis of generated data We first discuss some results obtained by the gradient-based approach, illustrated in Figure 3, for the specific surface area S_{AM} of the second interpolated parameter vector θ_2 between BM03 and BM10. For this exemplarily chosen reference parameter vector, the specific surface area S_{AM} of the corresponding model realization is equal to $1.10\,\mu\mathrm{m}^{-1}$. For $h = -0.1$, a value of $1.30\,\mu\mathrm{m}^{-1}$ is obtained, and for $h = -0.2$ a value of $1.52\,\mu\mathrm{m}^{-1}$. In the opposite direction of the gradient, the specific surface area S_{AM} shows slightly smaller changes, with values of $1.06\,\mu\mathrm{m}^{-1}$ for $h = 0.1$ and $1.00\,\mu\mathrm{m}^{-1}$ for $h = 0.2$. Moreover, as shown in Figure 5, the gradient-based approach enables the generation of a database comprising a variety of distinct morphologies with respect to further geometrical descriptors, where the volume fraction of AM ranges from 0.45 to 0.57, while that of SE ranges from 0.33 to 0.48. The mean geodesic tortuosity $\mu(\tau_{\mathrm{SE}})$ of SE reaches values from 1.08 to 1.18. In contrast, the mean geodesic tortuosity $\mu(\tau_{\mathrm{AM}})$ of AM is comparatively low, which is expected, as the AM phase is highly connected due to the dense and tightly packed AM particles, implying that the shortest paths through the AM are almost straight [57]. Higher AM tortuosity would be undesirable, as it would correspond to a poorly connected AM network. With the same reasoning, it can be explained that most values of the AM constrictivity

β_{AM} are clustered between 0.9 and 1. In comparison, the constrictivity β_{SE} of SE, as well as the specific surface areas S_{AM} and S_{SE} of AM and SE, exhibit wider value ranges, reflecting greater variability of the simulated image data with respect to these geometrical descriptors.

Predicting the M-factor via regression models As shown in Figure 5e, the M-factors M_{AM} and M_{SE} exhibit a good spread for both AM and SE, providing a suitable basis for regression models. The noticeable difference in the ranges of M_{AM} and M_{SE} can be explained by the fact that the M-factor is bounded from above by the corresponding volume fraction. Although the ranges of M_{AM} and M_{SE} overlap, the volume fraction $\varepsilon_{\mathrm{AM}}$ of AM extends to higher values than that of SE, which in turn allows M_{AM} to reach higher values.

The evaluation of the M-factor both through various prediction models and numerical simulations shows that the volume fraction alone is insufficient to predict the M-factor. As shown in Figure 6a, this results in a low coefficient of determination, $R^2 = 0.300$ for AM, highlighting that other geometrical descriptors beyond the volume fraction significantly influence transport. In contrast, for SE, the higher value of $R^2 = 0.843$ is achieved, indicating that the volume fraction is the dominant factor controlling ionic conductivity in this phase. This observation is supported by the fact that the coefficient c_1 in $\widehat{M}_1$ is higher for SE, specifically $c_1 = 2.32$, than for AM, where we have $c_1 = 1.98$, see Table 5. Incorporating constrictivity and mean geodesic tortuosity, as done for $\widehat{M}_2$, yields significantly improved results—an effect that is far more pronounced for AM than for SE. This is expected, as both descriptors directly impact transport pathways, particularly in the more complex microstructure of AM. The fact that the coefficient of determination R^2 only increases slightly—by 0.009 for AM and by 0.03 for SE—suggests that including either the standard deviation of geodesic tortuosity or the constrictivity alongside the volume fraction and the mean geodesic tortuosity does not make a substantial difference. The models $\widehat{M}_3$ and $\widehat{M}_4$ show similar results for AM, with R^2 around 0.906 and MAPE = 1.68%, indicating that constrictivity provides limited additional information for predicting M. For the M-factors of SE, a small decrease in the R^2-value of 0.001 is observed, which may indicate that $\widehat{M}_4$ is slightly overfitting with respect to the training data. These findings imply that, for accurate prediction of M-factors, incorporating mean geodesic tortuosity is essential for AM, while for SE, the volume fraction alone captures most of the variability.

Note that some of the M-factor prediction models $\widehat{M}_1, \dots, \widehat{M}_4$ stated in Section 2.6 have already been investigated in the literature. Comparing the values of the coefficients $c_1, \dots, c_5$ computed there to those obtained in the present paper shows that there are some similarities. For model $\widehat{M}_3$, when considering the AM, c_3 is nearly identical to the value reported in [19] and only a minor difference can be observed in c_1, namely $c_1 = 1.18$ in [19] and $c_1 = 1.10$ in our case. Furthermore, when looking at the coefficients in Table 5, it becomes clear that the constrictivity only has a minor influence on the M-factor of AM as the corresponding coefficients are very small, i.e., $c_3 = -0.002$ for $\widehat{M}_2$ and $c_5 = -0.002$ for $\widehat{M}_4$. For SE, on the other hand, these coefficients are slightly higher with values of $c_3 = -0.09$ and $c_5 = -0.06$ indicating that the constrictivity is more important for the M-factor of SE than it is for that of AM. A similar phenomenon can be observed for the standard deviation $\sigma(\tau)$ of geodesic tortuosity τ. It seems to have only a minor influence on the M-factor of AM, with coefficient $c_3 = 0.03$ for $\widehat{M}_3$ and $\widehat{M}_4$, while for SE it amounts to $c_3 = 0.13$ for $\widehat{M}_3$ and $c_3 = 0.16$ for $\widehat{M}_4$.

The best trade-off between model simplicity and predictive precision is achieved by $\widehat{M}_3$ for both AM and SE, which incorporates the volume fraction as well as the mean and standard deviation of geodesic tortuosity. More precisely, for AM, the corresponding expression is given by

$$\widehat{M}_3 = 1.10\mu(\tau_{\mathrm{AM}})^{-19.60}\sigma(\tau_{\mathrm{AM}})^{0.03}\varepsilon_{\mathrm{AM}}^{0.24}, \tag{25}$$

and for SE by

$$\widehat{M}_3 = 3.99\mu(\tau_{\mathrm{SE}})^{-0.54}\sigma(\tau_{\mathrm{SE}})^{0.13}\varepsilon_{\mathrm{SE}}^{3.26}. \tag{26}$$

5 Conclusions

In the present paper, an approach is introduced that enables systematic variation of model parameters and thus the generation of a large database of virtual 3D ASSB cathode microstructures that have not yet been observed experimentally. For these microstructures, effective macroscopic properties such as ionic and electronic conductivity can be computed by means of numerical simulations. This framework enables the investigation of structure-property relationships by identifying correlations between effective transport properties and geometrical descriptors, while avoiding the high costs and time consuming procedures associated with the production and imaging of experimental samples.

To implement this virtual materials testing framework, a stochastic microstructure model is employed. Specifically, a simplified version of the model introduced in [37] is used, which is based on excursion sets of random fields and calibrated with the help of a generative adversarial framework (GAN).

Usually, when generating a large database of virtual microstructures using a stochastic 3D model, the volume fraction of each material phase is directly controlled by a model parameter and can therefore be intentionally adjusted [19]. However, typically it is difficult to specify parameters of stochastic models such that generated microstructures exhibit predefined values for other descriptors—especially those closely linked to transport processes, for example geodesic tortuosity and constrictivity. This applies in particular to more complex stochastic models, as is the case with the model used in the present paper. Combining interpolation between fitted parameter vectors, corresponding to three experimentally measured images, with a gradient-based approach allows this limitation to be overcome. For each interpolated point, the difference quotient with respect to a specific geometrical descriptor can be evaluated for each entry of a parameter vector $\theta \in \Theta$ and thus leads to an approximation of the gradient. This enables a systematic variation of cathode microstructures with respect to those geometrical descriptors.

Computing ionic and electronic conductivity for all generated structures using GeoDict enables investigation of structure-property relationships. More specifically, several regression models, involving different combinations of geometrical descriptors, were calibrated to a training dataset to quantify the influence of volume fraction, geodesic tortuosity and constrictivity on effective transport properties of the simulated cathode microstructures. For each fitted regression model, the mean absolute percentage error, and the coefficient of determination R^2 are computed for a test dataset. The results obtained show that the volume fraction has a substantially greater influence on the M-factor of SE than on that of AM. Furthermore, the mean geodesic tortuosity also proves to be an important geometrical descriptor when examining its effect on ionic and electronic conductivity. In contrast, constrictivity and standard deviation of geodesic tortuosity appear to have a smaller impact on these effective transport properties. Nevertheless, at least one of these two geometrical descriptors, together with the volume fraction and the mean geodesic tortuosity, is required to obtain well-fitting regression models. The best trade-off between model complexity and predictive precision is given by $\widehat{M}_3$ for both material phases, AM and SE, comprising the volume fraction as well as the mean and standard deviation of geodesic tortuosity, see Eqs. (25) and (26).

In a forthcoming study, the structure-property relationships derived in the present paper will be used for inverse microstructure design, which aims to identify optimized values of relevant geometrical descriptors required to achieve a desired set of effective material properties, such as maximized ionic conductivity, sufficient electronic conductivity, and minimized tortuosity. Then, instead of predicting effective properties for given microstructures, structure-property relationships, such as those given in Eqs. (25) and (26), will be numerically inverted by formulating an optimization problem. The goal is to identify optimized geometrical descriptor ranges and model parameters that lead to the desired macroscopic transport properties.

Acknowledgement

This research is funded by the German Federal Ministry of Research, Technology and Space (BMFTR) under grant number 03XP0562.

References

[1] R. Korthauer. *Lithium-Ion Batteries: Basics and Applications*. Springer, 2018.

[2] S. Passerini, D. Bresser, A. Moretti, and A. Varzi. *Batteries: Present and Future Energy Storage Challenges*. J. Wiley & Sons, 2020.

[3] H. Aziam, B. Larhrib, C. Hakim, N. Sabi, H. B. Youcef, and I. Saadoune. Solid-state electrolytes for beyond lithium-ion batteries: A review. *Renewable and Sustainable Energy Reviews*, 167:112694, 2022.

[4] J. Chen, J. Wu, X. Wang, A. Zhou, and Z. Yang. Research progress and application prospect of solid-state electrolytes in commercial lithium-ion power batteries. *Energy Storage Materials*, 35:70–87, 2021.

[5] H.-D. Lim, J.-H. Park, H.-J. Shin, J. Jeong, J. T. Kim, K.-W. Nam, H.-G. Jung, and K. Y. Chung. A review of challenges and issues concerning interfaces for all-solid-state batteries. *Energy Storage Materials*, 25:224–250, 2020.

[6] J. Janek and W. G. Zeier. Challenges in speeding up solid-state battery development. *Nature Energy*, 8: 230–240, 2023.

[7] Y. Ren, T. Danner, A. Moy, M. Finsterbusch, T. Hamann, J. Dippell, T. Fuchs, M. Müller, R. Hoft, A. Weber, , L. A. Curtiss, P. Zapol, M. Klenk, A. T. Ngo, P. Barai, B. C. Wood, R. Shi, L. F. Wan, T. W. Heo, M. Engels, J. Nanda, F. H. Richter, A. Latz, V. Srinivasan, J. Janek, J. Sakamoto, E. D. Wachsman, and D. Fattakhova-Rohlfing. Oxide-based solid-state batteries: a perspective on composite cathode architecture. *Advanced Energy Materials*, 13:2201939, 2023.

[8] D. Zhang, X. Cao, D. Xu, N. Wang, C. Yu, W. Hu, X. Yan, J. Mi, B. Wen, L. Wang, and L. Zhang. Synthesis of cubic Na_3SbS_4 solid electrolyte with enhanced ion transport for all-solid-state sodium-ion batteries. *Electrochimica Acta*, 259:100–109, 2018.

[9] A. Asheri, S. Rezaei, V. Glavas, and B.-X. Xu. Microstructure impact on chemo-mechanical fracture of polycrystalline lithium-ion battery cathode materials. *Engineering Fracture Mechanics*, 309:110370, 2024.

[10] T.-S. Vu, M.-Q. Ha, D.-N. Nguyen, V.-C. Nguyen, Y. Abe, T. Tran, H. Tran, H. Kino, T. Miyake, K. Tsuda, and H.-C. Dam. Towards understanding structure–property relations in materials with interpretable deep learning. *npj Computational Materials*, 9:215, 2023.

[11] P. Marmet, L. Holzer, T. Hocker, H. Bausinger, J. G. Grolig, A. Mai, J. M. Brader, and G. K. Boiger. Multiscale-multiphysics model for optimization of novel ceramic MIEC solid oxide fuel cell electrodes. *The International Journal of Multiphysics*, 18:58–83, 2024.

[12] M. Clausnitzer, R. Mücke, F. Al-Jaljouli, S. Hein, M. Finsterbusch, T. Danner, D. Fattakhova-Rohlfing, O. Guillon, and A. Latz. Optimizing the composite cathode microstructure in all-solid-state batteries by structure-resolved simulations. *Batteries & Supercaps*, 6:e202300167, 2023.

[13] J. Park, K. T. Kim, D. Y. Oh, D. Jin, D. Kim, Y. S. Jung, and Y. M. Lee. Digital twin-driven all-solid-state battery: unraveling the physical and electrochemical behaviors. *Advanced Energy Materials*, 10:2001563, 2020.

[14] Z. Liu, S. Bai, S. Burke, J. N. Burrow, R. Geurts, C.-J. Huang, C. Jiao, H.-B. Lee, Y. S. Meng, L. Novák, B. Winiarski, J. Wang, K. Wu, and M. Zhang. FIB-SEM: emerging multimodal/multiscale characterization techniques for advanced battery development. *Chemical Reviews*, 125:5228–5281, 2025.

[15] J. Carazo, C. Sorzano, J. Otón, R. Marabini, and J. Vargas. Three-dimensional reconstruction methods in single particle analysis from transmission electron microscopy data. *Archives of Biochemistry and Biophysics*, 581:39–48, 2015.

[16] E. Maire and P. J. Withers. Quantitative X-ray tomography. *International Materials Reviews*, 59:1–43, 2014.

[17] J. Ohser and F. Mücklich. *Statistical Analysis of Microstructures in Materials Science*. J. Wiley & Sons, 2000.

[18] O. Stenzel, O. Pecho, L. Holzer, M. Neumann, and V. Schmidt. Big data for microstructure-property relationships: A case study of predicting effective conductivities. *AIChE Journal*, 63:4224–4232, 2017.

[19] B. Prifling, M. Röding, P. Townsend, M. Neumann, and V. Schmidt. Large-scale statistical learning for mass transport prediction in porous materials using 90,000 artificially generated microstructures. *Frontiers in Materials*, 8:786502, 2021.

[20] M. Neumann, O. Stenzel, F. Willot, L. Holzer, and V. Schmidt. Quantifying the influence of microstructure on effective conductivity and permeability: Virtual materials testing. *International Journal of Solids and Structures*, 184:211–220, 2020.

[21] S. W. Nam, D. Lee, E. Choi, J. Yeom, S. H. Choi, and D.-J. Yoo. Spotlighting composite cathode heterogeneity: challenges and strategies for all-solid-state batteries. *ACS Applied Energy Materials*, 8:6876–6888, 2025.

[22] J. S. Kim, S. Jung, H. Kwak, Y. Han, S. Kim, J. Lim, Y. M. Lee, and Y. S. Jung. Synergistic halide-sulfide hybrid solid electrolytes for ni-rich cathodes design guided by digital twin for all-solid-state li batteries. *Energy Storage Materials*, 55:193–204, 2023.

[23] J. Y. Kim, J. Park, M. J. Lee, S. H. Kang, D. O. Shin, J. Oh, J. Kim, K. M. Kim, Y.-G. Lee, and Y. M. Lee. Diffusion-dependent graphite electrode for all-solid-state batteries with extremely high energy density. *ACS Energy Letters*, 5(9):2995–3004, 2020.

[24] G. Gaiselmann, M. Neumann, V. Schmidt, O. Pecho, T. Hocker, and L. Holzer. Quantitative relationships between microstructure and effective transport properties based on virtual materials testing. *AIChE Journal*, 60:1983–1999, 2014.

[25] N. Jeziorski and C. Redenbach. Stochastic geometry models for texture synthesis of machined metallic surfaces: sandblasting and milling. *Journal of Mathematics in Industry*, 14:17, 2024.

[26] L. Théodon, J. Debayle, and C. Coufort-Saudejaud. Vox-storm: A stochastic 3D model based on a dual voxel-mesh architecture for the morphological characterization of aggregates. *Powder Technology*, 444:119983, 2024.

[27] O. Furat, L. Petrich, D. P. Finegan, D. Diercks, F. Usseglio-Viretta, K. Smith, and V. Schmidt. Artificial generation of representative single li-ion electrode particle architectures from microscopy data. *npj Computational Materials*, 7:105, 2021.

[28] M. Neumann, S. E. Wetterauer, M. Osenberg, A. Hilger, P. Gräfensteiner, A. Wagner, N. Bohn, J. R. Binder, I. Manke, T. Carraro, and V. Schmidt. A data-driven modeling approach to quantify morphology effects on transport properties in nanostructured NMC particles. *International Journal of Solids and Structures*, 280: 112394, 2023.

[29] M. Neumann, M. Osenberg, A. Hilger, D. Franzen, T. Turek, I. Manke, and V. Schmidt. On a pluri-gaussian model for three-phase microstructures, with applications to 3D image data of gas-diffusion electrodes. *Computational Materials Science*, 156:325–331, 2019.

[30] P. Marmet, L. Holzer, T. Hocker, V. Muser, G. K. Boiger, M. Fingerle, S. Reeb, D. Michel, and J. M. Brader. Stochastic microstructure modeling of SOC electrodes based on a pluri-gaussian method. *Energy Advances*, 2: 1942–1967, 2023.

[31] G. Inoue and M. Kawase. Numerical and experimental evaluation of the relationship between porous electrode structure and effective conductivity of ions and electrons in lithium-ion batteries. *Journal of Power Sources*, 342:476–488, 2017.

[32] S. Föhst, S. Osterroth, F. Arnold, and C. Redenbach. Influence of geometry modifications on the permeability of open-cell foams. *AIChE Journal*, 68:e17446, 2022.

[33] S. Daubner and B. Nestler. Microstructure characterization of battery materials based on voxelated image data: Computation of active surface area and tortuosity. *Journal of The Electrochemical Society*, 171:120514, 2024.

[34] B. Prifling, D. Westhoff, D. Schmidt, H. Markoetter, I. Manke, V. Knoblauch, and V. Schmidt. Parametric microstructure modeling of compressed cathode materials for li-ion batteries. *Computational Materials Science*, 169:109083, 2019.

[35] O. Stenzel, O. Pecho, L. Holzer, M. Neumann, and V. Schmidt. Predicting effective conductivities based on geometric microstructure characteristics. *AIChE Journal*, 62:1834–1843, 2016.

[36] I. J. Goodfellow, J. Pouget-Abadie, M. Mirza, B. Xu, D. Warde-Farley, S. Ozair, A. Courville, and Y. Bengio. Generative adversarial nets. *Advances in Neural Information Processing Systems*, 27, 2014.

[37] O. Furat, S. Weber, A. Dufter, J. Schubert, R. Rekers, M. Luczak, E. Glatt, A. Wiegmann, J. Janek, A. Bielefeld, and V. Schmidt. Generative adversarial framework to calibrate excursion set models for the 3D morphology of all-solid-state battery cathodes. *Advanced Intelligent Systems*, page 2500572, 2025.

[38] P. Minnmann, J. Schubert, S. Kremer, R. Rekers, S. Burkhardt, R. Ruess, A. Bielefeld, F. H. Richter, and J. Janek. Editors' choice—visualizing the impact of the composite cathode microstructure and porosity on solid-state battery performance. *Journal of The Electrochemical Society*, 171:060514, 2024.

[39] T. Zou, J. Shi, M. Wang, and C. Lin. Inverse design of structured electrodes in lithium metal batteries: Integrated high-throughput phase-field modeling and machine learning. *Advanced Functional Materials*, page e12788, 2025.

[40] S. N. Chiu, D. Stoyan, W. S. Kendal, and J. Mecke. *Stochastic Geometry and Its Applications*. J. Wiley & Sons, 2013.

[41] K. Schladitz, J. Ohser, and W. Nagel. Measuring intrinsic volumes in digital 3D images. In *Discrete Geometry for Computer Imagery: 13th International Conference, DGCI 2006, Szeged, Hungary, October 25-27, 2006. Proceedings 13*, pages 247–258. Springer, 2006.

[42] M. Neumann, C. Hirsch, J. Staněk, V. Beneš, and V. Schmidt. Estimation of geodesic tortuosity and constrictivity in stationary random closed sets. *Scandinavian Journal of Statistics*, 46:848–884, 2019.

[43] D. Jungnickel. *Graphs, Networks and Algorithms*. Springer, 2005.

[44] P. Soille. *Morphological Image Analysis: Principles and Applications*, volume 2. Springer, 1999.

[45] B. Münch and L. Holzer. Contradicting geometrical concepts in pore size analysis attained with electron microscopy and mercury intrusion. *Journal of the American Ceramic Society*, 91:4059–4067, 2008.

[46] J. Nocedal and S. J. Wright. *Numerical Optimization*. Springer, 2026.

[47] Z. Zhang, Y. Shao, B. Lotsch, Y.-S. Hu, H. Li, J. Janek, L. F. Nazar, C.-W. Nan, J. Maier, M. Armand, and L. Chen. New horizons for inorganic solid state ion conductors. *Energy & Environmental Science*, 11: 1945–1976, 2018.

[48] A. Fick. Ueber Diffusion. *Annalen der Physik*, 170:59–86, 1855.

[49] S. Torquato. *Random Heterogeneous Materials: Microstructure and Macroscopic Properties*. Springer, 2002.

[50] S. J. Cooper, M. Kishimoto, F. Tariq, R. S. Bradley, A. J. Marquis, N. P. Brandon, J. A. Kilner, and P. R. Shearing. Microstructural analysis of an LSCF cathode using in situ tomography and simulation. *Electrochemical Society Transactions*, 57:2671–2678, 2013.

[51] B. Prifling, M. Ademmer, F. Single, O. Benevolenski, A. Hilger, M. Osenberg, I. Manke, and V. Schmidt. Stochastic 3D microstructure modeling of anodes in lithium-ion batteries with a particular focus on local heterogeneity. *Computational Materials Science*, 192:110354, 2021.

[52] Math2Market GmbH. GeoDict Simulation Software, Release 2026, 2026. URL `https://doi.org/10.30423/release.geodict2026`.

[53] A. Wiegmann and A. Zemitis. EJ-HEAT: A fast explicit jump harmonic averaging solver for the effective heat conductivity of composite materials. Fraunhofer ITWM Report 94, Fraunhofer Institute for Industrial Mathematics (ITWM), Kaiserslautern, Germany, 2006.

[54] A. Vadakkepatt, B. Trembacki, S. R. Mathur, and J. Y. Murthy. Bruggeman's exponents for effective thermal conductivity of lithium-ion battery electrodes. *Journal of the Electrochemical Society*, 163:A119–A130, 2016.

[55] D.-W. Chung, M. Ebner, D. R. Ely, V. Wood, and R. Edwin García. Validity of the bruggeman relation for porous electrodes. *Modelling and Simulation in Materials Science and Engineering*, 21:074009, 2013.

[56] P. Virtanen, R. Gommers, T. E. Oliphant, M. Haberland, T. Reddy, D. Cournapeau, E. Burovski, P. Peterson, W. Weckesser, J. Bright, S. J. van der Walt, M. Brett, J. Wilson, K. J. Millman, N. Mayorov, A. R. J. Nelson, E. Jones, R. Kern, E. Larson, C. J. Carey, İ. Polat, Y. Feng, E. W. Moore, J. VanderPlas, D. Laxalde, J. Perktold, R. Cimrman, I. Henriksen, E. A. Quintero, C. R. Harris, A. M. Archibald, A. H. Ribeiro, F. Pedregosa, and P. van Mulbregt. Scipy 1.0: fundamental algorithms for scientific computing in python. *Nature Methods*, 17:261–272, 2020.

[57] S.-Y. Park, J. Jeong, and H.-C. Shin. Geometrical effect of active material on electrode tortuosity in all-solid-state lithium battery. *Applied Sciences*, 12:12692, 2022.